Materials Today Physics 22 (2022) 100584

Contents lists available at ScienceDirect

Materials Today Physics

journal homepage: https://www.journals.elsevier.com/materials-today-physics

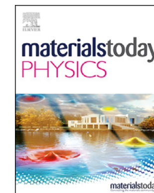

Nano-composite phase-change antimony thin film for fast and persistent memory operations

Yimin Chen [a, b, 1], Bin Chen [c, 1], Lei Sun [a], Wenhao Leng [a], Yingjie Meng [a], Chenjie Gu [a, b], Yuanlin Chen [c], Tao Song [c], Jiaen Huang [c], Junqiang Wang [d], Guoxiang Wang [a], Xiang Shen [a, b, **], Feng Rao [c, *]

[a] *Laboratory of Infrared Material and Devices & Key Laboratory of Photoelectric Materials and Devices of Zhejiang Province, Advanced Technology Research Institute, Ningbo University, Ningbo, 315211, China*
[b] *Department of Microelectronic Science and Engineering, School of Physical Science and Technology, Ningbo University, Ningbo, 315211, China*
[c] *College of Materials Science and Engineering, Shenzhen University, Shenzhen, 518060, China*
[d] *CAS Key Laboratory of Magnetic Materials and Devices & Zhejiang Province Key Laboratory of Magnetic Materials and Application Technology, Ningbo Institute of Materials Technology & Engineering, Chinese Academy of Sciences, Ningbo, 315201, China*

A R T I C L E I N F O

Article history:
Received 29 September 2021
Received in revised form
12 November 2021
Accepted 24 November 2021
Available online 30 November 2021

Keywords:
Phase-change memory materials
Antimony
Nano composite
Crystallization kinetics
Working memory.

A B S T R A C T

Elemental Sb phase-change material (PCM) has to be diminished to nanometer in thickness to guarantee non-volatile memory storage. Integrating ultrathin Sb films poses great challenges in manufacturing high-density phase-change random-access memory (PCRAM) chips. Here, we introduce another feasible approach of utilizing nano-composite Sb–SiO_2 PCM, for which we demonstrate superior phase-change properties of faster crystallization speed and better data retention ability over the conventional $Ge_2Sb_2Te_5$ compound. These two seemingly conflicting features of the Sb–SiO_2 are reconciled by an obvious fragile-to-strong crossover in crystallization kinetics of the supercooled Sb liquids via nanosize confinements, enabling the more suffocated atomic diffusion near room temperature and the comparable crystal growth at elevated temperatures to the $Ge_2Sb_2Te_5$. The nanosize confinements also catalyze heterogeneous nucleation remarkably, therefore speeding up the SET operation of the Sb–SiO_2-based PCRAM device by over two orders of magnitude as compared to the $Ge_2Sb_2Te_5$-based one. In addition, owning the potentials to accomplish low-drift and long-life memory programming, the nano-composite Sb–SiO_2 PCMs hold great promise to be employed for working memory and neuromorphic computing applications.

© 2021 Elsevier Ltd. All rights reserved.

1. Introduction

The rapid development of artificial intelligence, big data analysis, supercomputing, and internet of things drives the revolution of current computing system based on classic von Neumann architecture, where the frequent and massive data shuttling between the core processor and hierarchical memories costs lots of intercommunicating time and energy consumption through limited bandwidth [1,2]. Emerging non-volatile memory (NVM) technologies offer a feasible route to overcome such a bottleneck by either serving as a storage-class memory [3–5] to mitigate hierarchical performance mismatches or unifying calculation and storage at memory cell sites to facilitate in-memory computations [6–9]. Among existing NVMs, phase-change random access memory (PCRAM), which encodes digital data via swift and reversible structural transformations between the amorphous and crystalline phases of chalcogenide phase-change materials (PCMs), is the leading candidate in these two renovating regards [10–13]. Commercialized PCRAM devices utilize flagship $Ge_2Sb_2Te_5$ (GST)-like compounds as the storage medium that can execute phase transformations within tens to hundreds of nanoseconds while store the data reliably for tens of years at ambient temperatures [14,15]. However, current PCRAM technology still faces miscellaneous challenges in achieving high-speed, high-accuracy, and long-life device properties [16–18], which mainly come from the intrinsic material properties of the GST-like PCMs.

* Corresponding author.
** Corresponding author.
E-mail addresses: shenxiang@nbu.edu.cn (X. Shen), fengrao@szu.edu.cn (F. Rao).
[1] These authors contributed equally to this work.

https://doi.org/10.1016/j.mtphys.2021.100584
2542-5293/© 2021 Elsevier Ltd. All rights reserved.

The presence of Ge element triggers a large fraction of homopolar Ge—Ge bonds and tetrahedral atomic motifs in the amorphous GST networks [19], hindering the rearrangement into octahedrally-configured structures for swift crystallization. Also due to the pronounced stochasticity in the nucleation process of GST [20,21], its PCRAM devices usually exhibit quite sluggish SET (crystallization) operations. Even when the feature size of memory cell is shrunken considerably into sub 10 nm scale, the fastest SET operation still costs ~30 ns [17], which is much slower than the criterion of working memories (sub ~1—10 ns) [22,23]. Meanwhile, the abundance of homopolar Ge—Ge bonds and tetrahedral motifs in amorphous GST decreases gradually upon structural relaxation, giving rise to the annihilation of localized defect states and/or a widened electronic band gap, which results in a striking and steady increase in device resistance of the RESET (amorphous) state [24,25]. This would unavoidably degrade the data consistency in multibit storage or parallel computing. Furthermore, upon large-bias or repeated operations, the GST-like PCMs suffer from severe phase segregation that originates from the field-assisted long-distance migration of Ge(Sb) and Te elements in opposite directions due to their different electronegativities [26], causing poor programming reliabilities and short service life of the PCRAM devices.

Obviously, removing Ge element is an effective way to address above issues. In a ~4 nm-thick Sb_2Te_3 bridge-type device, SET time can be shortened to ~1 ns [27], accompanied by a noticeably relieved resistance drift [12]. Elaborately designed Sc-doped Sb_2Te_3 PCMs accommodate robust Sc—Te heterogeneous nucleation sites, suppressing the stochastic nucleation thus speeding up the SET operation into sub-ns regime [23,28]. Further simplifying the stoichiometry leads to the monoatomic Sb PCM that is regarded as a potential candidate to alleviate the phase segregation for a longer cycling endurance [29]. Note that 'bulk' Sb films (>~10 nm in thickness) crystallize spontaneously at room temperature, impeding non-volatile data storage for practical use. Doping offers a promising route to improve its thermals stability, in the cost of slowing down SET speed [30,31]. Nevertheless, reducing the Sb film thickness to sub ~5 nm in a PCRAM device can effectively enhance the data stability of its RESET state [29,32], meanwhile retaining reliable multilevel states with pretty low resistance drift [32]. Nonetheless adopting such slim Sb films in a vertical integration scheme to fabricate high-density PCRAM devices would pose great challenges on manufacturing techniques involving nanogap-filling or nondestructive etching process. Moreover, the phase-change kinetics and thermodynamics at such an ultrathin scale should be substantially altered with respect to the bulk PCM cases, therefore it would be a tough task to fine tuning the bilateral dielectric confinements of the ultrathin Sb film to acquire desired phase-change performances.

To circumvent these difficulties that will be confronted when utilizing the ultrathin Sb in PCRAM devices, in this work, we provide an alternative approach of nano-composite Sb—SiO_2 PCM, where the phase-changeable Sb regions are nanosize-confined within an amorphous matrix of non-phase-changeable SiO_2 areas, adjusting the crystallization kinetics essentially to achieve fast but persistent phase-change performances. The Sb—SiO_2-based PCRAM devices can perform much faster SET operations than the GST-based ones, because the Sb—SiO_2 PCM has enhanced heterogeneous nucleation rates and slightly higher crystal growth velocities at elevated temperatures, whereas it also possesses superior data retention abilities over the GST, owing to a more suffocated atomic diffusivity at low temperatures. We believe that these two 'conflicting' features found in the Sb—SiO_2 PCM must be reconciled by a fragile-to-strong (FTS) crossover in kinetics, while the supercooled GST liquids do not own such a peculiarity. Our work thus suggests to revisit the phase-change kinetics of many nano-composite PCMs, aiming to optimize the material compositions for superior device properties to promote the developments of both working and storage-class memories.

2. Experimental methods

2.1. Film preparation and characterization

The Sb—SiO_2 films were prepared by co-sputtering SiO_2 and Sb targets (with purity of 99.99%) under high vacuum at room temperature. The base and working pressures were ~8 × 10^{-3} and ~3 mTorr, respectively. The GST films were prepared by sputtering the alloy target (with purity of 99.99%). We employed x-ray fluorescence (XRF, AXIOS, Malvern Panalytical) spectrometer to determine the exact composition of Sb—SiO_2 PCM: $Sb_{69.7}(SiO_2)_{30.3}$. The ~120 nm-thick Sb—SiO_2 and GST films for temperature-dependent sheet-resistance measurements were deposited on the SiO_2/Si substrates. On top of the PCM layers, a ~10 nm-thick SiO_2 layer was *in-situ* deposited to avoid the surficial oxidation. The sheet resistance-temperature curve was characterized via a homemade heating platform with an accuracy of ±0.1 C. The specimen for high-resolution transmission electron microscopy (HRTEM, JEOL JEM-2100 F) measurements was directly deposited on carbon grids. The morphology of ~250 °C annealed Sb—SiO_2 films (~12 nm in thickness with a ~3 nm-thick SiO_2 capping layer) was confirmed by HRTEM at a high tension of 200 kV. The chemistry state of the Sb—SiO_2 films was examined by x-ray photoelectron spectroscopy (XPS, Thermo Scientific K-Alpha+).

2.2. PCRAM device fabrication and electrical measurement

The PCRAM devices were fabricated on a Si substrate with ~300 nm-thick thermally oxidized SiO_2 layer which acts as the thermal and electrical insulation. The ~10 nm-thick Ti and ~100 nm-thick W layers were successively deposited on the SiO_2/Si substrate by sputtering Ti and W target (with purity of 99.99%), serving as the bottom electrode of the device. Another 50 nm-thick SiO_2 layer was subsequently deposited as a protective layer, and a number of via pores were constructed in this SiO_2 layer by electron-beam lithography (EBL, Raith eLINE Plus) and following inductively coupled plasma (ICP, Oxford Instruments plasma 100) reactive ion etching processes. Then an active region with the geometry of ~100 × 100 × 50 nm^3 was formed and surrounded by the dielectric SiO_2 walls. Another ultraviolent lithography process was utilized to pattern the top electrode before *in-situ* depositing the PCM layer and top W electrode. Then the excess materials of non-device areas were removed by lift-off process. The electrical performance of the PCRAM devices were characterized by Keithley 2400C source meter and Tektronix AWG5202 pulse generator for resistance measurement and nanoseconds voltage pulses generation (with a minimum width of ~4 ns), respectively.

2.3. Flash differential scanning calorimetry (FDSC) measurements

Power-compensation DSC was performed by using a Mettler-Toledo FDSC 1 instrument with the sensor chips (USF-1) each containing working and reference areas. The ~200 nm-thick Sb—SiO_2 films for the FDSC measurements were deposited on crystalline NaCl substrates. Small Sb—SiO_2 flakes were scraped off from the substrate and then transferred onto the working area of the sensor chip. The heating rates Φ varied from 20 to 40,000 K s^{-1}. At each Φ, measurements were repeated at least 3 times for low Φ and 5—10 times for high Φ, as the values of the crystallization temperature become more scattered at high Φ. Thermal lag and temperature calibration of the FDSC are evaluated in detail in the

Supplementary Information. Detailed methodology of Kissinger fitting can be found in our previous work [33]. The viscosity model used in this work is illustrated in the Supplementary Information. Since the Sb–SiO_2 flakes were only one-side capped, it is appropriate to compare the FDSC results with those of uncapped GST films [34].

3. Results and discussion

3.1. Structural transformation and thermal stability of amorphous Sb–SiO_2 films

Due to the explosive-crystallization nature of bulk Sb films [35], stabilizing the amorphous phase has for long time been an intriguing but challenging task [29]. At room temperature, the amorphous phase in pure Sb films only exists below ~5 nm in film thickness [29,32], while in our Sb–SiO_2 case, a much thicker sample (~120 nm) is still capable of retaining the amorphous phase, exhibiting an initially high sheet resistance of ~10^6 Ω/□ (Fig. 1A). The as-deposited amorphous Sb–SiO_2 film crystallizes at ~198 °C, i.e., the crystallization temperature (T_c), (Fig. 1A), accompanied by a sharp drop in sheet resistance at around the T_c. In comparison, the GST film of the same thickness has a lower T_c ~172 °C. Also note that the amorphous Sb–SiO_2 film possesses a higher activation energy of crystallization (E_a) ~2.88 eV than that of the GST film ~2.21 eV (Fig. 1B). As a consequence, the amorphous Sb–SiO_2 film displays significantly better ten-year data retention ability (~100.2 °C) than that of the GST competitor (~82.8 °C) (Fig. 1B).

One may intuitively attribute the strengthened amorphous phase of the Sb–SiO_2 film to just a simple doping phenomenon, as many Si or O doped PCMs possess enhanced thermal stabilities [36] that should be ascribed to the formation of additional rigid chemical bonds between Si/O and phase-change elements. To clarify whether this is also valid in the Sb–SiO_2 case, we carried out XPS measurements to investigate the bonding status of its amorphous phase. The electronegativity of O (3.5) is considerably larger than that of Si (1.8), therefore Sb–O bonds should be more prone to form than Sb–Si bonds if both Si and O dopants are introduced into Sb simultaneously. We firstly checked the situation of the Sb–SiO_2 surface, using the naturally oxidized Sb as a reference (the black curve in Fig. 1C). Apart from the binding energy of the metallic Sb–Sb bonds, i.e., $3d_{5/2}$ (528.2 eV) and $3d_{3/2}$ (537.6 eV) [37], another two peaks emerge at 530.5 and 539.9 eV, matching well with binding energy values of Sb–O $3d_{5/2}$ and $3d_{3/2}$ in Sb_2O_3 [38]. Then we *in-situ* etched the film for ~20 nm in XPS chamber and characterized the chemistry again (the red curve in Fig. 1C). For the inner part of the Sb–SiO_2 film, only the peaks for metallic Sb–Sb bonds can be observed, implying that the nano-composited Sb

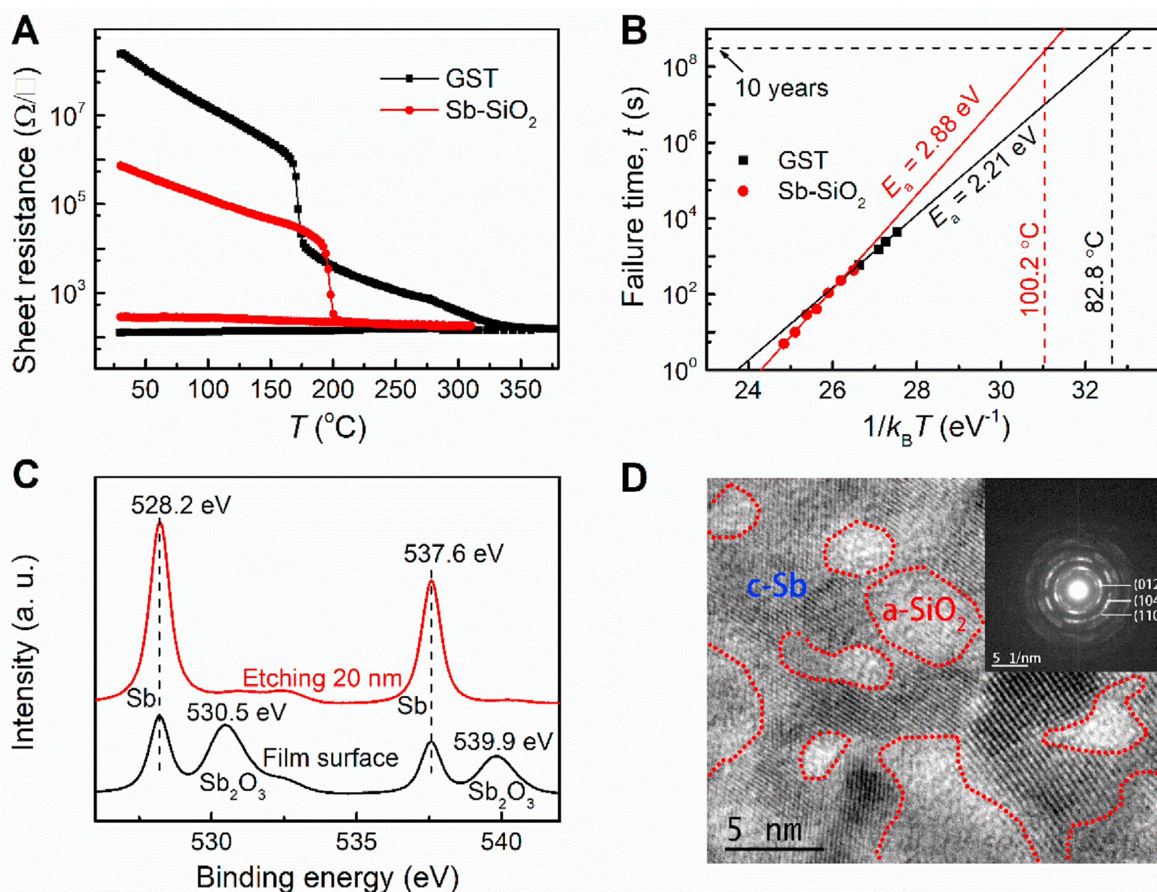

Fig. 1. (A) Temperature dependent sheet resistance of the as-deposited ~120 nm-thick GST and Sb–SiO_2 thin films sandwiched by SiO_2 layers. The heating rate is 60 K min^{-1}. T_c is defined as the temperature where the maximum 1st order of derivative occurs in the resistance-temperature curve. (B) Data retention abilities for the ~150 nm-thick GST and Sb–SiO_2 thin films sandwiched by SiO_2 layers. The data were fitted using Arrhenius equation $t = A\exp(E_a/k_BT)$, where t is the time to failure when resistance of amorphous films, at a certain isothermal heating temperature, becomes half of its initial value; A is a proportionality constant; E_a is the activation energy, and k_B is the Boltzmann constant. (C) XPS spectrum of the Sb–SiO_2 thin films. The sample was not capped with SiO_2 layer, therefore the surface layer (black curve) was oxidized showing peaks belonged to the Sb_2O_3, while the inner materials (red curve) is avoided from oxidation. (D) Bright field HRTEM image of the 250 °C-annealed ~12 nm-thick Sb–SiO_2 films. Areas circled in red denote for the amorphous SiO_2 regions, surrounding crystalline Sb nanocrystals. The inset shows the corresponding SAED pattern.

areas may contain a very marginal concentration of Si or O element. It is the severe surficial oxidation under the circumstance of no caping layer that causes the appearance of rich Sb—O contents in the upper part of the Sb—SiO_2 film, while in a normal (protected) case, the Sb and SiO_2 regions inside the Sb—SiO_2 film should be spatially well separated.

We then conducted TEM observations to further verify such a micro morphology of the Sb—SiO_2 film. To better distinguish the SiO_2 and Sb regions, we annealed the as-deposited specimen at 250 °C for 3 min to turn amorphous Sb areas into crystalline (Fig. 1D), whereas the SiO_2 regions remain amorphous, shown as the brighter areas in the bright field TEM image (redly circled in Fig. 1D). The selected area electron diffraction (SAED) pattern exhibits sharp diffraction rings, matching well with the hexagonal Sb lattice (R 3(_) m, space group 166, $a = b = 4.30$ Å, $c = 11.22$ Å [39]) and confirming the polycrystalline nature of the annealed Sb—SiO_2 thin film. The amorphous SiO_2 areas can serve as nano-confinements restricting the Sb areas into nanoparticle-like shapes at the diameters ranging between ~5 and 20 nm. Akin to the thickness reduction, the geometrical miniaturization and confinement in nano scale together help to remarkably improve the amorphous stability of the Sb. Interestingly, we also found that the amorphous Sb—SiO_2 film has a pretty stable resistance state upon aging for ~800 s, showing a small drift coefficient v (~0.004) that is much lower than that of the amorphous GST counterpart (~0.031) (Fig. S1 in the Supplementary Information).

3.2. SET speed of Sb—SiO_2 and GST PCRAM devices

Note that due to the pretty high melting point (T_m), SiO_2 is thermally robust to retain its microstructure even being heated to ~1,300 K [40], far beyond the T_m of PCMs, i.e., ~900 K. Therefore, the SiO_2 nano-areas can mainly serve as the non-phase changeable confinements that will not essentially degrade the phase-change performances, for instance, the PCRAM device based on a nano-composite GST-SiO_2 shows a comparable endurance (10^7 cycles) with conventional GST one [41]. However, the nano-confinements can exert substantial influence on the crystallization behaviors. We therefore measured the SET speed of the Sb—SiO_2 and GST PCRAM devices (Fig. 2A). The mushroom-type PCRAM device has a contact area of ~100 × 100 nm^2 between the PCMs and bottom electrode. Electrical pulses with fixed width but increasing voltage magnitude were applied to SET (crystallize) the devices. The GST device can be fully crystallized under the SET bias ranging from ~3.5 to ~6.0 V, corresponding to the SET time from 50 to 6 ns (Fig. 2B). As a comparison, the Sb—SiO_2 device with identical geometry can reach the SET state at a much lower voltage bias (~1.7—~2.3 V) with analogous pulse width of 50 to 6 ns (Fig. 2C). A faster SET speed of 4 ns can be achieved by the Sb—SiO_2 devices, under a little larger SET voltage bias ~2.5 V.

Comparison of the SET speed values as a function of SET voltage between the two devices is shown in Fig. 2D. It is clear that at ~2.5—3.0 V, the Sb—SiO_2 device can be ~2 orders of magnitude faster than the GST counterpart. Such a faster crystallization nature of Sb—SiO_2 PCM seems to conflict with its thermally stabler amorphous phase. The latter may be originated from the suffocated atomic diffusion near room temperature caused by the SiO_2 confinements, whereas the atomic mobility may also be weakened at high crystallization temperatures, slowing down the crystal growth. It is worth reminding that, as a growth-dominated PCM, bulk Sb has a rather low nucleation rate during crystallization [42]. If the crystal growth and nucleation momentums are both restricted, how can the Sb—SiO_2 PCM crystallize that faster than the GST? We need to clarify the kinetics-related puzzle throughout the whole temperature range of supercooled liquid regime via FDSC analyses.

3.3. Crystallization kinetics of Sb—SiO_2 film

The FDSC studies have successfully unraveled the crystallization kinetics in many PCMs [34,43,44]. Heating rates ranging (Φ) from 20 to 40,000 K s^{-1} were carried out to crystallize the as-deposited ~200 nm-thick Sb—SiO_2 thin film flakes. Typical FDSC traces with background subtracted are represented in Fig. 3A, where increasing the Φ from 20 to 40,000 K s^{-1} shifts the crystallization peak temperature (T_p) from ~493 to ~544 K. The dependence of T_p on the Φ, which allows us to analyze the crystallization kinetics, is then depicted in the Kissinger plot (Fig. 3B). The T_p data of GST derived via FDSC [34] and conventional DSC [45] are also plotted here for comparison. The Sb—SiO_2 films present a considerably rigorous linear relation, abiding by the Arrhenius behavior even when the Φ reaches the maximum of 40,000 K s^{-1}. In contrast, the data of GST films deviate from the Arrhenius behavior since very low Φ (~100 K s^{-1}), above which super-Arrhenius behavior is observed with decreasing crystallization activation energy (proportional to the slope of Kissinger plot). Similar to Sc-doped Sb_2Te_3 [43] and AgInSbTe [46] PCMs, the broad temperature regime of Arrhenius behavior in the Sb—SiO_2 films is a strong indication of the FTS crossover in the viscosity η. Therefore, the generalized MYEGA model intrinsically consisting of FTS crossover, with the help of Johnson-Mehl-Avrami-Kolmogorov (JMAK) crystallization theory, was adopted to model FDSC traces (with details of the methodology shown in the Supplementary Information).

Fitting the Kissinger plot (solid curves in Fig. 3B) permits us to reveal the η (equation S3 in the Supplementary Information) of the supercooled PCM liquids. Fig. 3C illustrates the temperature dependence of the η for supercooled Sb—SiO_2 and GST liquids between glass transition temperature (T_g) and T_m. The η of GST at T_m via simulation [47] is also depicted in the figure (the diamond in Fig. 3C), which agrees well with the data we derived. Note that the T_g is determined as the temperature where the η reaches 10^{12} Pa s, resulting in the value of T_g as 423 and 378 K for Sb—SiO_2 and GST, respectively. The fragility m, defined as the slope of the viscosity at T_g, namely, $m = d[\log_{10}\eta(T)]/d(T_g/T)|_{T=T_g}$, is determined to be ~55 for the Sb—SiO_2 supercooled liquids, much lower than that of the GST (m ~102).

In the light of the relations between the η and the T (temperature), supercooled liquids are classified into two categories: strong liquids such as silica follow Arrhenius behavior in the whole temperature regime, while fragile liquids like o-terphenyl obey super-Arrhenius behavior [48]. Thus, the strong liquids display a consistent activation energy for viscosity (E_η) while the E_η of fragile liquids increases when the T is approaching T_g, indicating a severe viscosity drop when the temperature is elevated above T_g. Obviously, GST is more fragile than Sb—SiO_2 as approaching T_g. In the temperature below $1000/T = 1.75$, i.e., $T <$ ~571 K, the η of Sb—SiO_2 is several orders of magnitude larger than GST, implying strong suffocation of atomic diffusivity in the Sb—SiO_2 supercooled liquids. But at elevated temperatures (>~600 K), its η sharply decreases to equivalent values to GST, allowing fast atomic diffusivity for crystal growth.

This enlarged contrast in crystallization kinetics is mainly originated from the FTS crossover of Sb—SiO_2 system. The FTS crossover can be quantitatively scrutinized via evaluating $E_\eta = k_B d\ln(\eta/\eta_0)/d(1/T)$, with k_B the Boltzmann constant. Above $T_g/T = 0.85$ ($T <$ ~498 K), the E_η of Sb—SiO_2 reaches a plateau (Fig. 3D), indicating the complying of Arrhenius behavior in this low temperature range, while above this temperature, the E_η decreases continuously and becomes close to 0 at $T_g/T = 0.65$ (T ~650 K), implying a super-Arrhenius behavior with sharply increased atomic

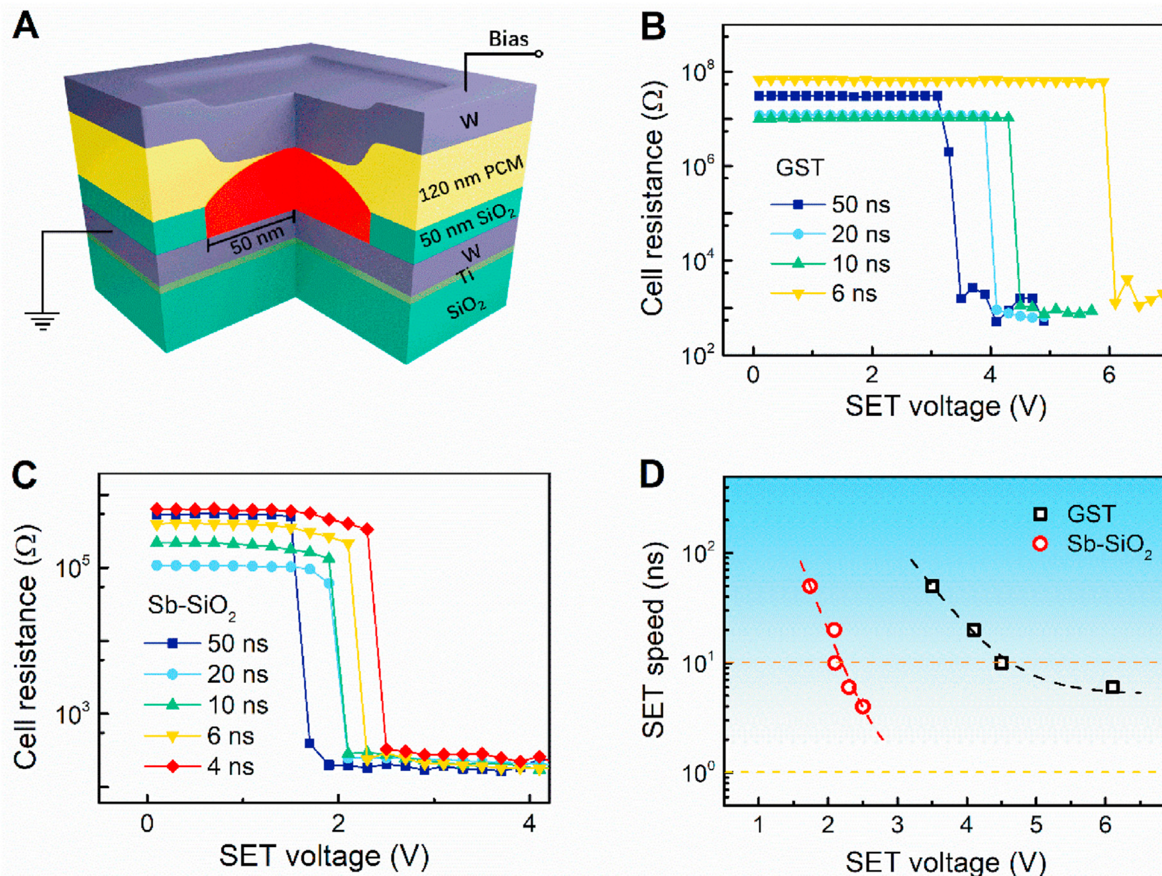

Fig. 2. (A) Schematic of the Sb–SiO_2- and GST-based PCRAM device with identical geometry, namely, ~120 nm-thick PCMs as the storage medium, ~100 × 100 nm^2 of contact area between the bottom W electrode and the PCMs, ~50 nm-thick SiO_2 dielectrics as confining walls acting as electrical and thermal insulating layer, and a ~40 nm-thick W layer as top electrode. The red mushroom inside the PCMs denotes for the active area where phase change occurs. (B)–(C) Cell resistance as a function of SET voltage under various SET pulse widths for GST- and Si–SiO_2-based PCRAM, respectively. (D) Comparison of SET speed between Sb–SiO_2- and GST-based PCRAM devices with identical geometry.

diffusivity (Fig. 3D). The inflection point of the E_η can be determined as the FTS crossover temperature (T_{FTS}). Contrarily, no FTS crossover is observed in the GST. The FTS crossover may stem from the increased Peierls distortion in short range and the formation of energetically favorable networks in medium range upon quenching the supercooled liquids [49,50]. The SiO_2 nano-confinements may help localizing electrons nearby the Sb–SiO_2 interfaces [51], deviating from the metavalent bonding scheme that prefers six equal bonds in much fragile Sb liquids at high temperatures [50]. With the FTS crossover, we simultaneously attain the superior thermal stability of amorphous Sb–SiO_2 at low temperatures approaching T_g and the considerably high atomic mobility at elevated temperatures, ensuring long data retention and fast crystal growth velocity, respectively. One need to note that a proper value of T_{FTS} is of necessity for acquire fast but persistent PCRAM performances, because a very high T_{FTS}, e.g., > ~500–600 K, may lead to viscous flow during SET operation (typically performing at ~600–700 K), while a too low T_{FTS}, e.g., < ~400 K, probably causes diffusive fluids resulting in substandard data retention ability.

3.4. Crystal growth and heterogeneous nucleation of Sb–SiO_2 film

Analogous to previous FDSC studies, crystallization process is simplified as that crystals grow in all the pre-existing nuclei [33,34]. After fitting the Kissinger plot in Fig. 3B, the crystal growth rate U as a function of temperature can be determined for Sb–SiO_2 and GST PCMs, as shown in Fig. 4A (see equation S1 and the detailed methodology in the Supplementary Information). The maximum growth rate (U_{max}) of Sb–SiO_2 is ~2.1 m s^{-1}, taking place at ~0.77 T_m (T ~691 K with T_m ~898 K in Fig. S2 in the Supplementary Information). The evidently lower U_{max} than previous value (~20–60 m s^{-1}) [42,52] indicates the slowing down of the atomic diffusivity by the SiO_2 confinements. As a comparison, the GST presents a comparable U_{max} ~1.9 m s^{-1}, occurring at ~0.70 T_m (T ~630 K), with T_m ~900 K [34]. The U_{max} of GST is in good agreement with previous data (~0.5–3 m s^{-1}) derived via various measurement such as FDSC and electrical measurement in PCRAM devices [33,34,53]. According to Stokes-Einstein relation, the atomic diffusivity D is inversely proportional to the η ($U \propto D \propto \eta^{-1}$). In PCMs, fractional Stokes-Einstein relation is ubiquitously observed in many systems [33,34,54], resulting in $U \propto D \propto \eta^{-\xi}$, with $\xi < 1$. The ξ is determined to be ~0.67 for both Sb–SiO_2 and GST through fitting. Due to the remarkably higher η of Sb–SiO_2 compared to the GST, a strikingly slower U is perceived below ~0.72 T_m (T < ~648 K), with the maximum difference ~5 orders of magnitude. Apparently, the ~2 orders of magnitude faster SET speed of Sb–SiO_2 device cannot only be ascribed to the crystal growth. Nucleation prior to crystal growth must lend the most credits to the faster crystallization of Sb–SiO_2.

We then calculated the nucleation rate of the Sb–SiO_2 and GST (with details seen in the Supplementary Information), as illustrated in Fig. 4B. In homogeneous situation, the steady-state nucleation rate (I^{ss}_{hom}) of Sb–SiO_2 is ~10 orders of magnitude lower than GST in the whole temperature range (~400–800 K). Besides, the effective

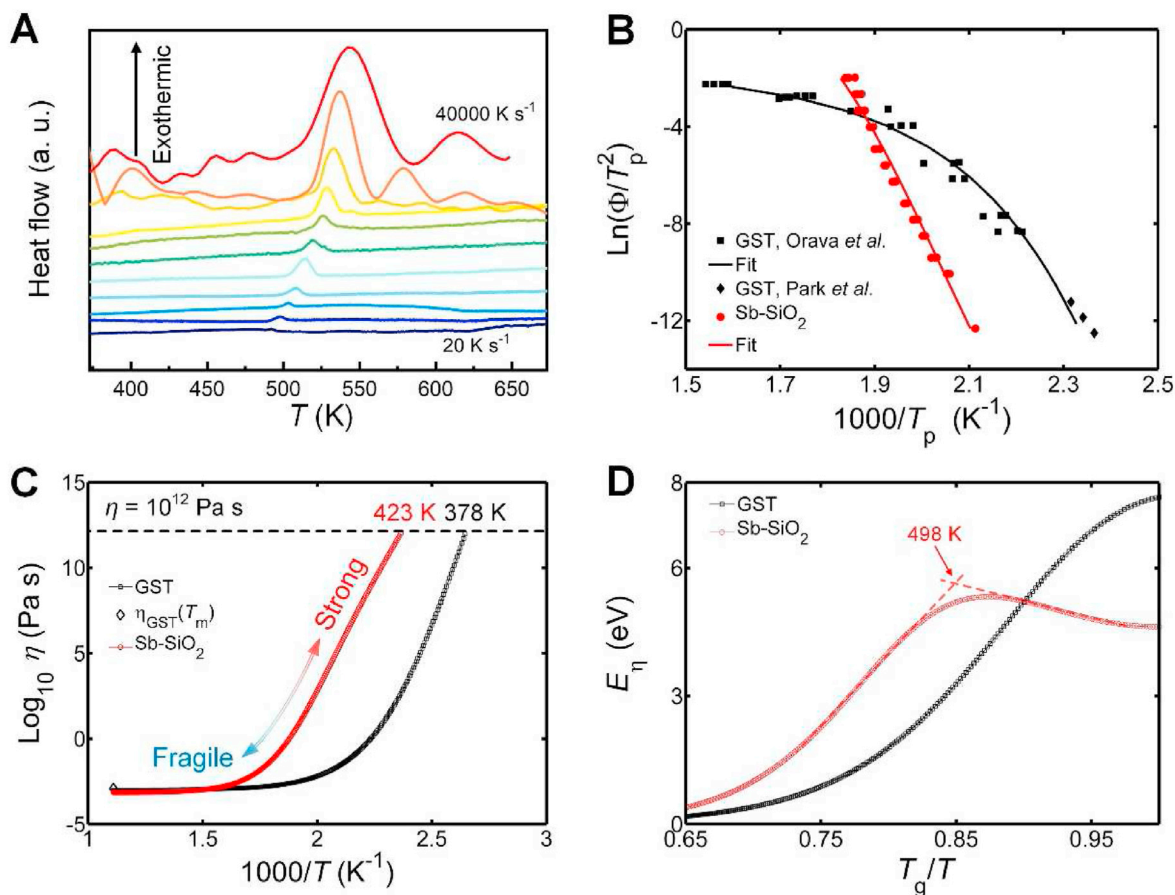

Fig. 3. (A) FDSC traces of ~200 nm-thick $Sb-SiO_2$ thin films with heating rate Φ ranging from 20 to 40,000 K s^{-1}. (B) Kissinger plot of $Sb-SiO_2$ and GST thin films, with the data for FDSC and conventional DSC obtained from previous works by Orava et al. [34]. and Park et al. [45]. (C) Temperature dependent viscosity η of $Sb-SiO_2$ and GST supercooled liquids, in between their glass transition temperature T_g and melting points T_m. The T_g is determined as the temperature where η reaches 10^{12} Pa s. The viscosity data at T_m for GST is derived from simulations [47], matching well with our data. (D) The viscosity activation energy (E_η) as a function of T_g scaled temperature, where E_η for $Sb-SiO_2$ reaches a plateau when quenched toward T_g, while that of GST increases monotonically. The fragile-to-strong crossover temperature is determined as 498 K for $Sb-SiO_2$.

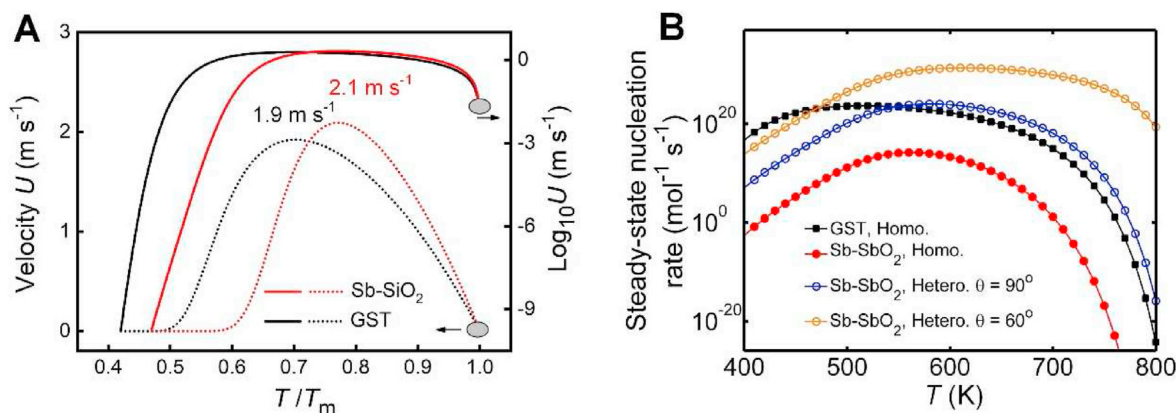

Fig. 4. (A) Crystal growth rate U in dependent of temperature of $Sb-SiO_2$ and GST supercooled liquids in the regime between T_g and T_m, with the maximum U (U_{max}) noted in the plot. (B) Steady-state nucleation rate (I^{SS}) of GST in homogeneous manner (abbreviated as Homo.) and $Sb-SiO_2$ in both homogeneous and heterogeneous (abbreviated as Hetero.) manners with the contact angle θ of 90 and 60.

time lag τ^* of $Sb-SiO_2$ is many orders of magnitude higher than the GST in this temperature regime (Fig. S3 in the Supplementary Information), indicating longer time required for the incubation of over-critical nuclei for subsequent crystal growth. The characteristics of comparable U_{max}, lower I^{ss}_{hom}, and higher τ^* in $Sb-SiO_2$ supercooled liquids obviously yield opposite results to the much faster SET speed attained. We are convinced that the heterogeneous nucleation [55] must play the crucial role in boosting the crystallization speed of $Sb-SiO_2$. The heterogeneous nucleation rate (I^{ss}_{het}) of $Sb-SiO_2$ with a wetting angle θ of 90 is comparable to GST at

temperature above ~550 K, below which it is still several orders of magnitude lower than the I^{ss}_{hom} of the GST. However, taking the $\theta = 60$ entails the larger I^{ss}_{het} of $Sb-SiO_2$ at above ~470 K. At the T ~600−700 K, the I^{ss}_{het} of $Sb-SiO_2$ is ~8−15 orders of magnitude higher than the I^{ss}_{hom} of GST. Moreover, the I^{ss}_{het} of $Sb-SiO_2$ keeps at a high value in the temperature range from ~600 to ~700 K, while the I^{ss}_{hom} of GST in the same temperature regime drops to ~8 orders of magnitude lower than its maximum value at T ~520 K. It is noticeable that the value of the θ here is just a conjecture to demonstrate the presence of heterogeneous nucleation in $Sb-SiO_2$. Our calculations strongly suggest that the SiO_2 nano-confining substances can catalyze the heterogeneous nucleation, remarkably promoting the nucleation rate prior to crystal growth that eventually boosts the SET operation in devices.

4. Conclusions

Bulk Sb films are volatile in storing amorphous state data. Via nanosize confinement using SiO_2, two seemingly irreconcilable features of fast crystallization speed and persistent amorphous state are simultaneously woven into the ~120 nm-thick nanocomposite $Sb-SiO_2$ PCM. An obvious FTS crossover in the nanoconfined supercooled Sb liquids suppresses the atomic diffusivity for low-temperature regime but retains high fluidity at elevated temperatures. Consequently, it becomes more viscous than GST for better data retention at room temperature, while its comparable viscosity with GST permits a close crystal growth rate (~2 m s^{-1}) at ~600−700 K. The SiO_2 confinements also substantially enhance the heterogenous nucleation rate of the $Sb-SiO_2$ nano-composite, facilitating an overall ~2 orders of magnitude faster SET operation speed against the GST device. Our work demonstrates a feasible approach of designing nano-composite PCMs via tailoring the kinetics to pursue fast but persistent phase-change properties for potential working memory applications.

Author contributions

Y. C. and W. L. prepared the phase-change films. Y. C. and J. W. performed FDSC measurements. L. S., Y. M., and C. G. fabricated the PCRAM devices. Y. C. and B. C. analyzed the FDSC data. B. C., Y. C., T. S., and J. H measured the electrical performance of the PCRAM devices. B. C. and F. R. wrote the paper with contribution from Y. C. All authors discussed the results and commented on the manuscript.

Declaration of competing interest

The authors declare that they have no known competing financial interests or personal relationships that could have appeared to influence the work reported in this paper.

Acknowledgements

F. Rao thanks the National Natural Science Foundation of China (52032006), the Basic and Applied Basic Research Foundation of Guangdong (2020B1515120008), and the Science and Technology Foundation of Shenzhen (JCYJ20180507182248605). X. Shen thanks the National Natural Science Foundation of China (61775111) and Zhejiang provincial Key R&D Program of China (2021C01025). Y. M. Chen thanks the National Natural Science Foundation of China (61904091), Zhejiang Provincial Natural Science Foundation of China (LY21F040003), and the K. C. Wong Magna Fund in Ningbo University. B. Chen thanks the National Natural Science Foundation of China (62004131).

Appendix A. Supplementary data

Supplementary data to this article can be found online at https://doi.org/10.1016/j.mtphys.2021.100584.

References

[1] H.-S.P. Wong, S. Salahuddin, Memory leads the way to better computing, Nat. Nanotechnol. 10 (2015) 191−194, https://doi.org/10.1038/nnano.2015.29.
[2] G. Kestor, R. Gioiosa, D.J. Kerbyson, A. Hoisie, Quantifying the energy cost of data movement in scientific applications. 2013 IEEE International Symposium on Workload Characterization, IISWC), 2013, pp. 56−65, https://doi.org/10.1109/IISWC.2013.6704670.
[3] R.F. Freitas, W.W. Wilcke, Storage-class memory: the next storage system technology, IBM J. Res. Dev.; Armonk. 52 (2008) 439−447.
[4] A. Sebastian, M. Le Gallo, R. Khaddam-Aljameh, E. Eleftheriou, Memory devices and applications for in-memory computing, Nat. Nanotechnol. 15 (2020) 529−544, https://doi.org/10.1038/s41565-020-0655-z.
[5] W. Zhang, R. Mazzarello, M. Wuttig, E. Ma, Designing crystallization in phase-change materials for universal memory and neuro-inspired computing, Nat. Rev. Mater. 4 (2019) 150−168, https://doi.org/10.1038/s41578-018-0076-x.
[6] G. Karunaratne, M. Le Gallo, G. Cherubini, L. Benini, A. Rahimi, A. Sebastian, In-memory hyperdimensional computing, Nat. Electron. 3 (2020) 327−337, https://doi.org/10.1038/s41928-020-0410-3.
[7] Q. Xia, J.J. Yang, Memristive crossbar arrays for brain-inspired computing, Nat. Mater. 18 (2019) 309−323, https://doi.org/10.1038/s41563-019-0291-x.
[8] J. Feldmann, N. Youngblood, C.D. Wright, H. Bhaskaran, W.H.P. Pernice, All-optical spiking neurosynaptic networks with self-learning capabilities, Nature 569 (2019) 208−214, https://doi.org/10.1038/s41586-019-1157-8.
[9] M. Xu, X. Mai, J. Lin, W. Zhang, Y. Li, Y. He, H. Tong, X. Hou, P. Zhou, X. Miao, Recent advances on neuromorphic devices based on chalcogenide phase-change materials, Adv. Funct. Mater. 30 (2020) 2003419, https://doi.org/10.1002/adfm.202003419.
[10] T. Tuma, A. Pantazi, M. Le Gallo, A. Sebastian, E. Eleftheriou, Stochastic phase-change neurons, Nat. Nanotechnol. 11 (2016) 693−699, https://doi.org/10.1038/nnano.2016.70.
[11] M. Le Gallo, A. Sebastian, R. Mathis, M. Manica, H. Giefers, T. Tuma, C. Bekas, A. Curioni, E. Eleftheriou, Mixed-precision in-memory computing, Nat. Electron. 1 (2018) 246−253, https://doi.org/10.1038/s41928-018-0054-8.
[12] K. Ding, J. Wang, Y. Zhou, H. Tian, L. Lu, R. Mazzarello, C. Jia, W. Zhang, F. Rao, E. Ma, Phase-change heterostructure enables ultralow noise and drift for memory operation, Science 366 (2019) 210−215, https://doi.org/10.1126/science.aay0291.
[13] D. Kuzum, R.G.D. Jeyasingh, B. Lee, H.-S.P. Wong, Nanoelectronic programmable synapses based on phase change materials for brain-inspired computing, Nano Lett. 12 (2012) 2179−2186, https://doi.org/10.1021/nl201040y.
[14] M. Wuttig, N. Yamada, Phase-change materials for rewriteable data storage, Nat. Mater. 6 (2007) 824−832, https://doi.org/10.1038/nmat2009.
[15] D. Ielmini, A.L. Lacaita, Phase change materials in non-volatile storage, Mater. Today 14 (2011) 600−607, https://doi.org/10.1016/S1369-7021(11)70301-7.
[16] D. Ielmini, D. Sharma, S. Lavizzari, AndreaL. Lacaita, Reliability impact of chalcogenide-structure relaxation in phase-change memory (PCM) cells—Part I: experimental study, IEEE Trans. Electron. Dev. 56 (2009) 1070−1077, https://doi.org/10.1109/TED.2009.2016397.
[17] I.S. Kim, S.L. Cho, D.H. Im, E.H. Cho, D.H. Kim, G.H. Oh, D.H. Ahn, S.O. Park, S.W. Nam, J.T. Moon, C.H. Chung, High performance PRAM cell scalable to sub-20nm technology with below 4F2 cell size, extendable to DRAM applications. 2010 Symposium on VLSI Technology, 2010, pp. 203−204, https://doi.org/10.1109/VLSIT.2010.5556228.
[18] W.W. Koelmans, A. Sebastian, V.P. Jonnalagadda, D. Krebs, L. Dellmann, E. Eleftheriou, Projected phase-change memory devices, Nat. Commun. 6 (2015) 1−7, https://doi.org/10.1038/ncomms9181.
[19] S. Caravati, M. Bernasconi, T.D. Kühne, M. Krack, M. Parrinello, Coexistence of tetrahedral- and octahedral-like sites in amorphous phase change materials, Appl. Phys. Lett. 91 (2007) 171906, https://doi.org/10.1063/1.2801626.
[20] J. Kalikka, J. Akola, R.O. Jones, Simulation of crystallization in $Ge_2Sb_2Te_5$: a memory effect in the canonical phase-change material, Phys. Rev. B 90 (2014) 184109, https://doi.org/10.1103/PhysRevB.90.184109.
[21] J. Kalikka, J. Akola, R.O. Jones, Crystallization processes in the phase change material $Ge_2Sb_2Te_5$: unbiased density functional/molecular dynamics simulations, Phys. Rev. B 94 (2016) 134105, https://doi.org/10.1103/PhysRevB.94.134105.
[22] D. Loke, T.H. Lee, W.J. Wang, L.P. Shi, R. Zhao, Y.C. Yeo, T.C. Chong, S.R. Elliott, Breaking the speed limits of phase-change memory, Science 336 (2012) 1566−1569, https://doi.org/10.1126/science.1221561.
[23] F. Rao, K. Ding, Y. Zhou, Y. Zheng, M. Xia, S. Lv, Z. Song, S. Feng, I. Ronneberger, R. Mazzarello, W. Zhang, E. Ma, Reducing the stochasticity of crystal nucleation to enable subnanosecond memory writing, Science 358 (2017) 1423−1427, https://doi.org/10.1126/science.aao3212.
[24] J.Y. Raty, W. Zhang, J. Luckas, C. Chen, R. Mazzarello, C. Bichara, M. Wuttig, Aging mechanisms in amorphous phase-change materials, Nat. Commun. 6 (2015) 1−8, https://doi.org/10.1038/ncomms8467.

[25] K. Konstantinou, F.C. Mocanu, T.-H. Lee, S.R. Elliott, Revealing the intrinsic nature of the mid-gap defects in amorphous Ge 2 Sb 2 Te 5, Nat. Commun. 10 (2019) 3065, https://doi.org/10.1038/s41467-019-10980-w.

[26] Y. Xie, W. Kim, Y. Kim, S. Kim, J. Gonsalves, M. BrightSky, C. Lam, Y. Zhu, J.J. Cha, Self-healing of a confined phase change memory device with a metallic surfactant layer, Adv. Mater. 30 (2018) 1705587, https://doi.org/10.1002/adma.201705587.

[27] K. Ding, B. Chen, F. Rao, Boosting crystallization speed in ultrathin phase-change bridge memory device using Sb_2Te_3, Mater. Sci. Semicond. Process. 134 (2021) 105999, https://doi.org/10.1016/j.mssp.2021.105999.

[28] K. Ding, B. Chen, Y. Chen, J. Wang, X. Shen, F. Rao, Recipe for ultrafast and persistent phase-change memory materials, NPG Asia Mater. 12 (2020) 1–10, https://doi.org/10.1038/s41427-020-00246-z.

[29] M. Salinga, B. Kersting, I. Ronneberger, V.P. Jonnalagadda, X.T. Vu, M.L. Gallo, I. Giannopoulos, O. Cojocaru-Mirédin, R. Mazzarello, A. Sebastian, Monatomic phase change memory, Nat. Mater. 17 (2018) 681–685, https://doi.org/10.1038/s41563-018-0110-9.

[30] M. Xu, B. Li, K. Xu, H. Tong, X. Cheng, M. Xu, X. Miao, Stabilizing amorphous Sb by adding alien seeds for durable memory materials, Phys. Chem. Chem. Phys. 21 (2019) 4494–4500, https://doi.org/10.1039/C8CP07446A.

[31] C. Qiao, K. Bai, M. Xu, S. Wang, C.-Z. Wang, K.-M. Ho, X. Miao, M. Xu, Ultrafast crystallization mechanism of amorphous $Ge_{15}Sb_{85}$ unraveled by pressure-driven simulations, Acta Mater. 216 (2021) 117123, https://doi.org/10.1016/j.actamat.2021.117123.

[32] F. Jiao, B. Chen, K. Ding, K. Li, L. Wang, X. Zeng, F. Rao, Monatomic 2D phase-change memory for precise neuromorphic computing, Appl. Mater. Today. 20 (2020) 100641, https://doi.org/10.1016/j.apmt.2020.100641.

[33] B. Chen, G.H. ten Brink, G. Palasantzas, B.J. Kooi, Crystallization kinetics of GeSbTe phase-change nanoparticles resolved by ultrafast calorimetry, J. Phys. Chem. C 121 (2017) 8569–8578, https://doi.org/10.1021/acs.jpcc.6b11707.

[34] J. Orava, A.L. Greer, B. Gholipour, D.W. Hewak, C.E. Smith, Characterization of supercooled liquid Ge2Sb2Te5 and its crystallization by ultrafast-heating calorimetry, Nat. Mater. 11 (2012) 279–283, https://doi.org/10.1038/nmat3275.

[35] N. Kaiser, Crystallization of amorphous antimony films, Thin Solid Films 116 (1984) 259–265, https://doi.org/10.1016/0040-6090(84)90445-0.

[36] F. Rao, Z. Song, Y. Cheng, M. Xia, K. Ren, L. Wu, B. Liu, S. Feng, Investigation of changes in band gap and density of localized states on phase transition for $Ge_2Sb_2Te_5$ and $Si_{3.5}Sb_2Te_3$ materials, Acta Mater. 60 (2012) 323–328, https://doi.org/10.1016/j.actamat.2011.09.015.

[37] P.M.ThM. van Attekum, J.M. Trooster, Bulk- and surface-plasmon-loss intensities in photoelectron, Auger, and electron-energy-loss spectra of Mg metal, Phys. Rev. B 20 (1979) 2335–2340, https://doi.org/10.1103/PhysRevB.20.2335.

[38] E.V. Benvenutti, Y. Gushikem, A. Vasquez, S.C. de Castro, G.A.P. Zaldivar, X-Ray photoelectron spectroscopy and mössbauer spectroscopy study of iron(III) and antimony(V) oxides grafted onto a silica gel surface, J. Chem. Soc., Chem. Commun. (1991) 1325–1327, https://doi.org/10.1039/C39910001325.

[39] D. Schiferl, C.S. Barrett, The crystal structure of arsenic at 4.2, 78 and 299°K, J. Appl. Crystallogr. 2 (1969) 30–36, https://doi.org/10.1107/S0021889869006443.

[40] K. Dick, T. Dhanasekaran, Z. Zhang, D. Meisel, Size-dependent melting of silica-encapsulated gold nanoparticles, J. Am. Chem. Soc. 124 (2002) 2312–2317, https://doi.org/10.1021/ja017281a.

[41] W. Czubatyj, S.J. Hudgens, C. Dennison, C. Schell, T. Lowrey, Nanocomposite phase-change memory alloys for very high temperature data retention, IEEE Electron. Device Lett. 31 (2010) 869–871, https://doi.org/10.1109/LED.2010.2051135.

[42] D. Dragoni, J. Behler, M. Bernasconi, Mechanism of amorphous phase stabilization in ultrathin films of monoatomic phase change material, Nanoscale (2021), https://doi.org/10.1039/D1NR03432D.

[43] B. Chen, Y. Chen, K. Ding, K. Li, F. Jiao, L. Wang, X. Zeng, J. Wang, X. Shen, W. Zhang, F. Rao, E. Ma, Kinetics features conducive to cache-type nonvolatile phase-change memory, Chem. Mater. 31 (2019) 8794–8800, https://doi.org/10.1021/acs.chemmater.9b02598.

[44] Y. Chen, G. Wang, L. Song, X. Shen, J. Wang, J. Huo, R. Wang, T. Xu, S. Dai, Q. Nie, Unraveling the crystallization kinetics of supercooled liquid GeTe by ultrafast calorimetry, Cryst. Growth Des. 17 (2017) 3687–3693, https://doi.org/10.1021/acs.cgd.7b00259.

[45] J. Park, M.R. Kim, W.S. Choi, H. Seo, C. Yeon, Characterization of amorphous phases of $Ge_2Sb_2Te_5$ phase-change optical recording material on their crystallization behavior, Jpn. J. Appl. Phys. 38 (1999) 4775, https://doi.org/10.1143/JJAP.38.4775.

[46] J. Orava, D.W. Hewak, A.L. Greer, Fragile-to-Strong crossover in supercooled liquid Ag-in-Sb-Te studied by ultrafast calorimetry, Adv. Funct. Mater. 25 (2015) 4851–4858, https://doi.org/10.1002/adfm.201501607.

[47] J. Akola, R.O. Jones, Structural phase transitions on the nanoscale: the crucial pattern in the phase-change materials $Ge_2Sb_2Te_5$ and GeTe, Phys. Rev. B 76 (2007) 235201, https://doi.org/10.1103/PhysRevB.76.235201.

[48] C.A. Angell, formation of glasses from liquids and biopolymers, Science 267 (1995) 1924–1935, https://doi.org/10.1126/science.267.5206.1924.

[49] F. Rao, W. Zhang, E. Ma, Catching structural transitions in liquids, Science 364 (2019) 1032–1033, https://doi.org/10.1126/science.aax6333.

[50] P. Zalden, F. Quirin, M. Schumacher, J. Siegel, S. Wei, A. Koc, M. Nicoul, M. Trigo, P. Andreasson, H. Enquist, M.J. Shu, T. Pardini, M. Chollet, D. Zhu, H. Lemke, I. Ronneberger, J. Larsson, A.M. Lindenberg, H.E. Fischer, S. Hau-Riege, D.A. Reis, R. Mazzarello, M. Wuttig, K. Sokolowski-Tinten, Femtosecond x-ray diffraction reveals a liquid–liquid phase transition in phase-change materials, Science 364 (2019) 1062–1067, https://doi.org/10.1126/science.aaw1773.

[51] X.-P. Wang, N.-K. Chen, X.-B. Li, Y. Cheng, X.Q. Liu, M.-J. Xia, Z.T. Song, X.D. Han, S.B. Zhang, H.-B. Sun, Role of the nano amorphous interface in the crystallization of Sb_2Te_3 towards non-volatile phase change memory: insights from first principles, Phys. Chem. Chem. Phys. 16 (2014) 10810–10815, https://doi.org/10.1039/C3CP55476G.

[52] B. Chen, J. Momand, P.A. Vermeulen, B.J. Kooi, Crystallization kinetics of supercooled liquid Ge–Sb based on ultrafast calorimetry, Cryst. Growth Des. 16 (2016) 242–248, https://doi.org/10.1021/acs.cgd.5b01151.

[53] A. Sebastian, M. Le Gallo, D. Krebs, Crystal growth within a phase change memory cell, Nat. Commun. 5 (2014), https://doi.org/10.1038/ncomms5314.

[54] S. Wei, Z. Evenson, M. Stolpe, P. Lucas, C.A. Angell, Breakdown of the Stokes-Einstein relation above the melting temperature in a liquid phase-change material, Sci. Adv. 4 (2018) eaat8632, https://doi.org/10.1126/sciadv.aat8632.

[55] S. Raoux, W. Welnic, D. Ielmini, Phase change materials and their application to nonvolatile memories, Chem. Rev. 110 (2010) 240–267.